J Adv Ceram

Research Article

Glass–ceramic joining of duplex SiC_f/SiC cladding tubes by localized rapid heating and its interfacial hydrothermal corrosion behavior

Chuang-Tian Zhan[1], Kun-Heng Huang[1], Jia-Pei Chen[1], Qu Ai[1], Yu Tian[1], Li-Xiang Wu[2], Yun Li[2], Wei-Ming Guo[1,✉], Yang Liu[2], Rong-Kun Yang[2], Jia-Xiang Xue[2,✉], Hua-Tay Lin[1,3,✉]

Cite this article: Zhan C-T, Huang K-H, Chen J-P, et al. *J Adv Ceram* 2026, **15**(4): 9221269. https://doi.org/10.26599/JAC.2026.9221269

ABSTRACT: SiC_f/SiC cladding tubes were joined to end plugs using Y_2O_3–Al_2O_3–SiO_2 (YAS) glass filler through localized rapid induction heating at 1400–1500 °C. The joint fabricated at 1450 °C exhibited a dense and uniform glass–ceramic interlayer with the highest nominal burst pressure of 70.3±10.0 MPa. A high joining temperature of 1500 °C suppressed the crystallization of the glass filler. Hydrothermal corrosion tests conducted at 360 °C and 18.6 MPa for 9 d revealed that both the interfaces on the end plug side and the cladding tube side were susceptible to corrosion, with more severe degradation occurring on the cladding tube side. The residual pyrolytic carbon (PyC) layer on the inner surface of the cladding tube facilitates indirect bonding between the filler and the tube. The resulting interfacial structure is unstable under hydrothermal conditions, leading to localized corrosion, void formation, and interfacial debonding. After corrosion, the joint retained a nominal burst pressure of 62.4±7.6 MPa. These results demonstrate that controlling interfacial structure and minimizing surface impurities are essential for improving the hydrothermal corrosion resistance and long-term reliability of SiC_f/SiC cladding joints.

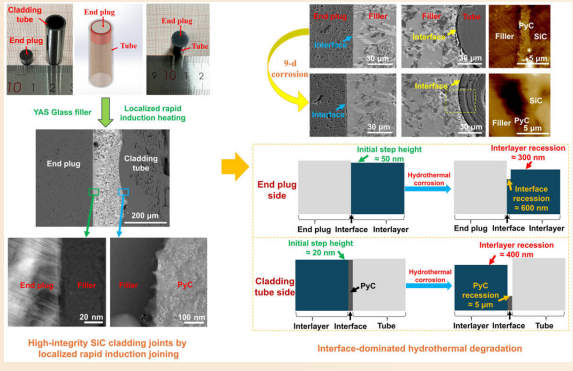

KEYWORDS: SiC_f/SiC; cladding tube; joining; hydrothermal corrosion; glass–ceramic

1 Introduction

SiC_f/SiC composites are regarded as one of the most promising candidates for accident-tolerant fuel cladding materials, owing to their potential to significantly enhance nuclear fuel safety under extreme accident scenarios [1–4]. However, a key challenge is achieving a reliable hermetic seal at the end of the tube to maintain leak-tightness and mechanical integrity throughout service [5,6]. To achieve reliable sealing of SiC_f/SiC cladding, various joining techniques have been developed, including precursor-derived joining, glass–ceramic joining, MAX-phase joining, nano-infiltration and transient eutectic (NITE)-phase joining, Si–C reaction bonding, metallic brazing, and diffusion bonding [7–14]. Among them, glass–ceramic joining is particularly attractive owing to its low-temperature, pressureless process and tunable thermal-expansion compatibility with SiC [8,15].

In glass–ceramic joining of SiC_f/SiC composite materials, the Y_2O_3–Al_2O_3–SiO_2 (YAS) glass is one of the most widely used fillers [16–18]. One of the primary advantages of the YAS glass system lies in its relatively good thermal expansion compatibility with SiC over a broad compositional design range, which is essential for minimizing residual stresses in joined structures. In addition, YAS glass–ceramic systems have been reported to exhibit favorable irradiation stability, making them attractive for nuclear-related applications [16]. Wang *et al.* [19] reported a shear strength of 51.7 MPa for SiC_f/SiC joints joined in a tube furnace at 1400 °C with a heating rate of 5 °C/min using a YAS glass filler. In this case, the interlayer consisted mainly of crystalline $Y_2Si_2O_7$, SiO_2, and $Al_6Si_2O_{13}$ phases together with residual glass, and the joints exhibited a mixed failure mode involving both the interlayer and the adjacent composite regions. Yang *et al.* [20] employed 3.0 wt% CaO-modified YAS glass to join SiC/SiC blocks in a tube furnace with a heating rate of 5 °C/min, achieving an apparent shear strength of 15.8±1.0 MPa at 1200 °C. The corresponding interlayer was reported to remain predominantly amorphous,

[1] School of Electromechanical Engineering, Guangdong University of Technology, Guangzhou 510006, China. [2] Nuclear Fuel and Materials Department, China Nuclear Power Technology Research Institute, Shenzhen 518026, China. [3] School of Materials and Environmental Engineering, Hunan University of Humanities, Science and Technology, Loudi 417000, China.

✉ Corresponding authors. E-mail: W.-M. Guo, guo1238@126.com; J.-X. Xue, jiaxiang_xue@163.com; H.-T. Lin, huataylin@comcast.net

Received: November 12, 2025; Revised: January 27, 2026; Accepted: February 20, 2026

without obvious crystallization. Although this joining approach demonstrated excellent gas-tightness for SiC cladding tube joints (no leakage under 15 MPa gas pressure for 72 h), quantitative push-out or hoop strength data were not reported. However, previous studies on YAS filler joining of SiC_f/SiC cladding tubes have mainly relied on conventional furnace heating at slow rates. The traditional methods often involve additional heat treatments at a crystallization temperature to form a distinct glass–ceramic interlayer, which enhances the high-temperature stability of the joint. However, such slow heating may cause excessive thermal exposure and potential damage to the cladding and its enclosed nuclear fuel [21]. Therefore, developing a localized and rapid heating technique to join SiC_f/SiC cladding tubes using a YAS filler capable of rapid crystallization is critical for ensuring efficient and safe sealing in nuclear applications.

Considering that SiC_f/SiC cladding tubes operate in hydrothermal environments, the hydrothermal corrosion resistance of sealing fillers is a critical criterion for evaluating their applicability. Ma *et al.* [22] conducted steam corrosion tests on YAS glass–ceramics at 1350 °C, showing that the material exhibits excellent corrosion resistance, with a weight loss of only 1.45% after 100 h of exposure. Ma *et al.* [23] further reported that YAS glass–ceramic coatings exhibited excellent corrosion and thermal-shock resistance in a 1350 °C water-oxygen atmosphere, remaining dense near the SiC_f/SiC substrate even after 100 thermal-shock cycles. These studies demonstrate that YAS glass-ceramics possess excellent resistance to hydrothermal corrosion. However, the corrosion behavior of the interface between the interlayer and the substrates of SiC_f/SiC cladding joints sealed with YAS glass remains insufficiently understood.

In this study, $39.7Y_2O_3$–$33.9Al_2O_3$–$26.4SiO_2$ (wt%) glass was employed as the filler to join SiC_f/SiC cladding tubes with SiC end plugs. To minimize thermal damage to the cladding and meet the requirements of nuclear sealing applications, a localized induction heating technique was adopted to achieve rapid and controlled joining, offering the advantage of confined heat input and reduced thermal exposure to the SiC_f/SiC cladding tube. The fabricated joints were subsequently subjected to hydrothermal corrosion tests under simulated pressurized water reactor conditions. Particular attention was given to the interfacial bonding behavior, hydrothermal corrosion resistance, and evolution of mechanical properties before and after exposure, aiming to provide fundamental insights for optimizing joint design and enhancing the long-term durability of SiC_f/SiC cladding systems.

2 Experimental

Figure 1(a) shows the SiC cladding tube and end plug used for joining. The tube has an outer diameter of 9.5 mm and a wall thickness of approximately 0.95 mm. Figure 1(b) shows the cross-sectional microstructure of the duplex SiC_f/SiC cladding tube, where the inner layer corresponds to the SiC_f/SiC composite (the blue arrow) and the outer layer is composed of chemical vapor deposition (CVD)-SiC (the red arrow). The end plugs were fabricated from pressureless-sintered SiC, with a height of 5.0 mm and a diameter of 7.4 mm.

The glass filler was prepared from SiO_2 (1 μm, > 99% purity, Shanghai Xiangtian Nano Materials Co., Ltd., China), Al_2O_3 (100 nm, > 99% purity, Daming Co., Ltd., China), and Y_2O_3 (3–6 μm, > 99% purity, Beijing Fandechen Technology Co., Ltd., China). These powders were weighed according to a mass ratio of $39.7Y_2O_3$:$33.9Al_2O_3$:$26.4SiO_2$, which has been verified to possess excellent high-temperature resistance and crystallization characteristics, and homogenized by ball milling for 24 h. The slurry was then subjected to rotary evaporation to obtain a mixed oxide powder. The mixed powder was melted at 1600 °C for 1 h and then quenched in water to obtain glass frit. The glass frit was milled using a planetary ball mill, followed by rotary evaporation and sieving through a 200-mesh screen to obtain the YAS glass powder.

The YAS glass powder was mixed with anhydrous ethanol (1 : 1 mass ratio) and ultrasonicated for 5 min to form a slurry, which was applied to the tube and the end plug. The preassembled specimens were joined at 1400, 1450, and 1500 °C using a custom-designed induction heating system that enabled localized rapid heating at 200 °C/min with a holding time of 10 min in an Ar atmosphere, where a graphite ring susceptor was inductively heated and served as a radiative heat source to selectively heat the joining region. Graphite felt was further employed as a thermal insulation layer to confine the heat input to the joint area. The resulting joints were designated J1400, J1450, and J1500, corresponding to the respective joining temperatures. Figure 2(a) shows a schematic of the cladding tube joint. Due to the inherent surface roughness of the inner wall and minor deviations in the roundness of the duplex SiC_f/SiC cladding tube, local variations in interlayer thickness may occur after assembly, resulting in slight differences at different circumferential positions. Overall, the interlayer thicknesses across different joining temperatures remain within a comparable range.

Hydrothermal corrosion tests were conducted in accordance with the standard EJ/T 1028-2014 using a high-pressure autoclave (HA-GYF-II, Jiangsu Hua'an Scientific Instruments Co., Ltd., China). Pure water was used as the corrosion medium, and no boric acid or LiOH was added to the water chemistry. At an ambient temperature of 23.7 °C, the pH value of the water was measured to be 6.7 using a calibrated pH meter (CT-6021A, Kedida, China). The dissolved oxygen content of the water was

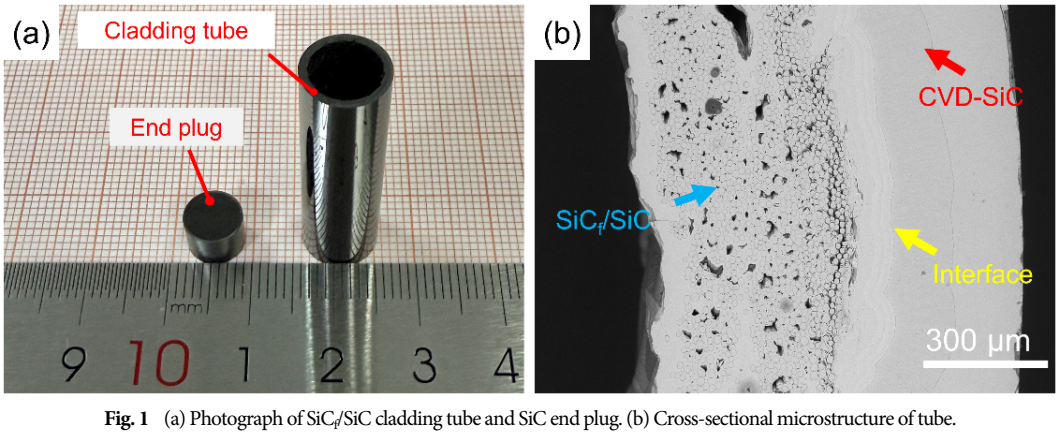

Fig. 1 (a) Photograph of SiC_f/SiC cladding tube and SiC end plug. (b) Cross-sectional microstructure of tube.

initially measured to be 15 ppm by the iodometric method (GB/T 7489-1987). During the corrosion tests, the water environment was deaerated according to the EJ/T 1028-2014 standard to control the dissolved oxygen content at a lower level. The joints were exposed to pure water at 360±5 °C under a pressure of 18.6±1.4 MPa for 9 days. A total of five joints for corrosion testing were prepared, with two joints utilized for microstructural tests. The results from these samples showed consistent corrosion behaviors, ensuring the reliability and reproducibility of the findings. The remaining three joints were used for end-plug push-out (EPPO) testing to calculate the nominal burst pressure.

Microstructural and compositional analyses were conducted using a scanning electron microscope (SEM; SU8220, Hitachi, Japan) equipped with an energy dispersive spectroscope (EDS; Oxford X-MaxN, Oxford, UK). Phase identification of the glass filler was carried out by an X-ray diffractometer (XRD; MiniFlex 600, Rigaku, Japan). It should be noted that the XRD patterns of the interlayer phases were obtained from YAS glass fillers that were heat-treated under exactly the same conditions as those used for joint fabrication, including the joining atmosphere and thermal profile. In addition, a bulk YAS glass specimen (~1.2 g) prepared at 1450 °C was separately subjected to hydrothermal corrosion in an autoclave. After corrosion, the aqueous solution was collected and analyzed by an inductively coupled plasma optical emission spectroscope (ICP-OES; Ultima Expert, HORIBA France SAS, France) to quantify the dissolved elemental species. The surface morphologies of the joint interfaces were examined by an atomic force microscope (AFM; Dimension Icon, Bruker, Germany). Cross-sectional interfacial structures were investigated by a transmission electron microscope (TEM; Talos F200X, Thermo Fisher, USA). The joining strength was evaluated through the EPPO test following ASTM C1862-17 using a universal testing machine (AGS-X-50KND, Shimadzu, Japan). The specimen for EPPO tests had a total length of 25 mm for the cladding tube, with an end plug inserted to a depth of 5 mm. The EPPO test configuration is illustrated in Fig. 2(b), and the nominal burst pressure (P_{NB}) was calculated using Eqs. (1) and (2):

$$P_{NB} = F_{PO}/A_F \tag{1}$$

$$A_F = \pi\left(\frac{d}{2}\right)^2 \tag{2}$$

where F_{PO} is the maximum push-out force (N), d is the diameter of the end-plug (mm), A_F is the cross-sectional area of the end plug (mm^2), and P_{NB} represents the nominal burst pressure of the joint (MPa).

3 Results and discussion

3.1 Joining of SiC_f/SiC cladding tubes with YAS glass filler

Figure 3(a) shows a low-magnification SEM image of the J1400 joint, where numerous crystalline phases are distributed within the interlayer. The interface between the interlayer and the end plug is well bonded without visible pores. In contrast, local voids are observed at the interface between the filler and the tube (red arrows in Fig. 3(a)). This difference is mainly attributed to the high surface roughness and pronounced topography of the inner surface of the tube, where the molten filler could not fully wet the surface at 1400 °C, leaving residual voids along the interface [24,25]. Figure 3(b) presents a high-magnification SEM image of the interlayer in the J1400 joint. The interlayer shows a typical glass–ceramic structure. The interlayer can be divided into four distinct regions (Fig. 3(b)): region 1 (spectrum 1) appears gray, region 2 (spectrum 2) is grayish-white, region 3 (spectrum 3) appears white, and region 4 (spectrum 4) is dark. The corresponding EDS results for these four regions are summarized in Table 1. Figure 4(a) shows the XRD pattern of the as-prepared YAS glass filler, while Fig. 4(b) presents the XRD pattern of the filler heat-treated under the same conditions as those used for joint fabrication at 1400 °C. It should be noted that although the crystallization peaks appear strong, they actually mask the amorphous background of the glass phase. In essence, the interlayer structure is a glass–ceramic composite, as confirmed by the microstructural analysis in Figs. 3(a) and 3(b). Spectrum 1 in Fig. 3(b), taken from the gray glassy region, has the composition listed in EDS point analyses in Table 1. Spectrum 2 corresponds to grayish-white equiaxed grains, with an atomic composition of Al : Y : O = 23.6 : 14.2 : 62.2, which is consistent with $Y_3Al_5O_{12}$ as identified by XRD. Spectrum 3 corresponds to white needle-like grains, with an atomic composition of Y : Si : O = 18.8 : 19.8 : 61.4. Based on the XRD results, this phase is identified as $Y_2Si_2O_7$, the predominant crystalline phase in the interlayer. Spectrum 4 corresponds to dark plate-like grains, with an Al : O atomic ratio of 40.8 : 59.2, which is consistent with α-Al_2O_3, as further confirmed by the XRD results.

Figure 3(c) shows the microstructure of the joint fabricated at 1450 °C. The glass–ceramic interlayer is dense and continuous, exhibiting well-bonded interfaces with both the SiC end plug and the SiC_f/SiC cladding tube, except for a few isolated pores. Compared with the J1400 joint, the interfacial bonding quality is markedly improved due to the higher joining temperature, which enhances the filler fluidity and wetting of the cladding surface [26]. It should be noted that the crystallized phases within the

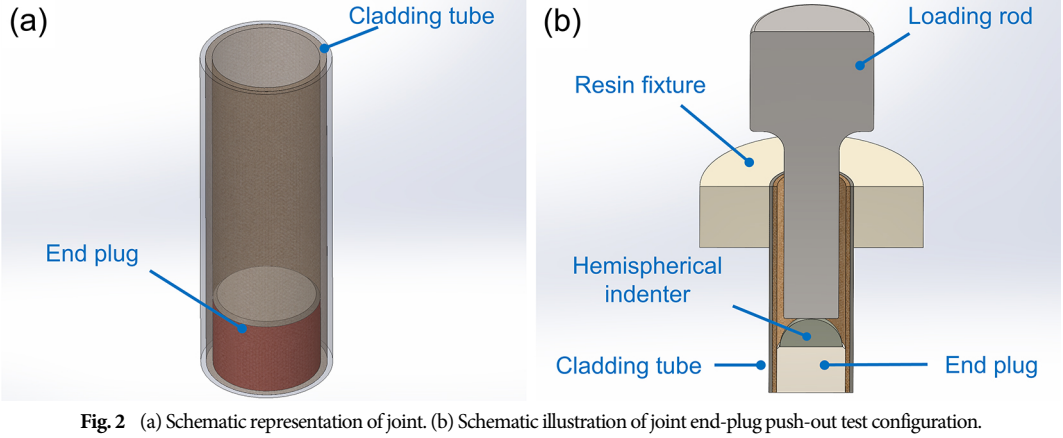

Fig. 2 (a) Schematic representation of joint. (b) Schematic illustration of joint end-plug push-out test configuration.

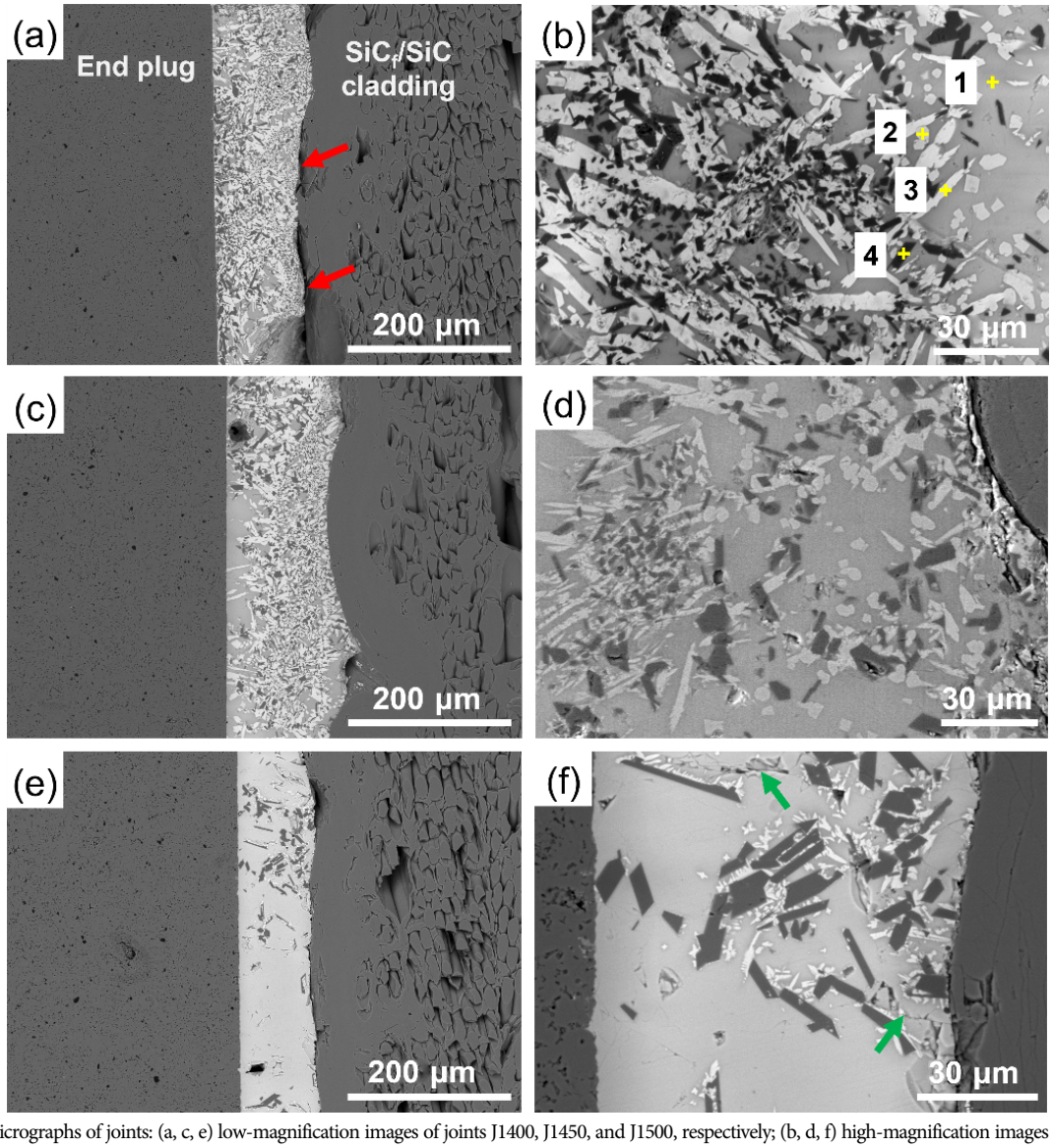

Fig. 3 SEM micrographs of joints: (a, c, e) low-magnification images of joints J1400, J1450, and J1500, respectively; (b, d, f) high-magnification images of interlayers in joints J1400, J1450, and J1500, respectively.

Table 1 EDS point analysis results for spectra 1, 2, 3, and 4 in the J1400 joint shown in Fig. 3

Spectrum	Atomic ratio of element (%)				Possible crystalline phase
	Al	Y	Si	O	
1	11.9±1.2	9.6±0.9	13.5±1.3	65.0±7.8	—
2	23.6±3.0	14.2±1.5	—	62.2±9.6	$Y_3Al_5O_{12}$
3	—	18.8±2.7	19.8±2.5	61.4±6.0	$Y_2Si_2O_7$
4	40.8±5.3	—	—	59.2±7.6	Al_2O_3

interlayer are not uniformly distributed (Fig. 3(c)). The crystallized phase tends to be more concentrated on the side closer to the tube. This may be related to the characteristics of the inner surface of the tube, such as its roughness, or the presence of pyrolytic carbon (PyC) on the inner surface, which could induce more pronounced crystallization behavior. Figure 3(d) presents a high-magnification SEM image of the interlayer. Similar to the J1400 joint, $Y_2Si_2O_7$, $Y_3Al_5O_{12}$, and Al_2O_3 crystalline phases are identified within the filler, consistent with the XRD results in Fig. 4(c).

Figure 3(e) shows the microstructure of the joint fabricated at 1500 °C. Both the end plug and the cladding tube exhibit well-bonded interfaces with the filler. However, the interlayer exhibits significant differences from the joints prepared at 1400 and 1450 °C. The glassy phase fraction increases noticeably, as evidenced by the much larger glassy matrix of the filler observed in Fig. 3(e) and the stronger amorphous background in the XRD pattern of Fig. 4(d). Figure 3(f) shows two crystalline phases, Al_2O_3 and $Y_2Si_2O_7$, which are identified from the XRD results. Compared with the J1450 joint (Fig. 3(d)), the J1500 joint contains a higher fraction of Al_2O_3. In addition, local microcracks are observed within the interlayer (green arrows in Fig. 3(f)), which are likely associated with aggravated local thermomechanical mismatch arising from the higher joining temperature and the uneven distribution of crystalline phases [27,28].

Among the three joining temperatures, the J1450 joint exhibits the most uniform and crack-free interlayer with a balanced crystallization state. To further clarify the interfacial bonding under these representative conditions, a TEM analysis was conducted on the interface between the end plug and the interlayer of the J1450 joint, as shown in Fig. 5. Figure 5(a) shows a cross-sectional TEM image of the interface between the end plug and the interlayer. The boundary is sharp, and no continuous reaction layer is visible. The selected area electron diffraction (SAED) patterns from the SiC and interlayer sides (Figs. 5(b) and 5(c))

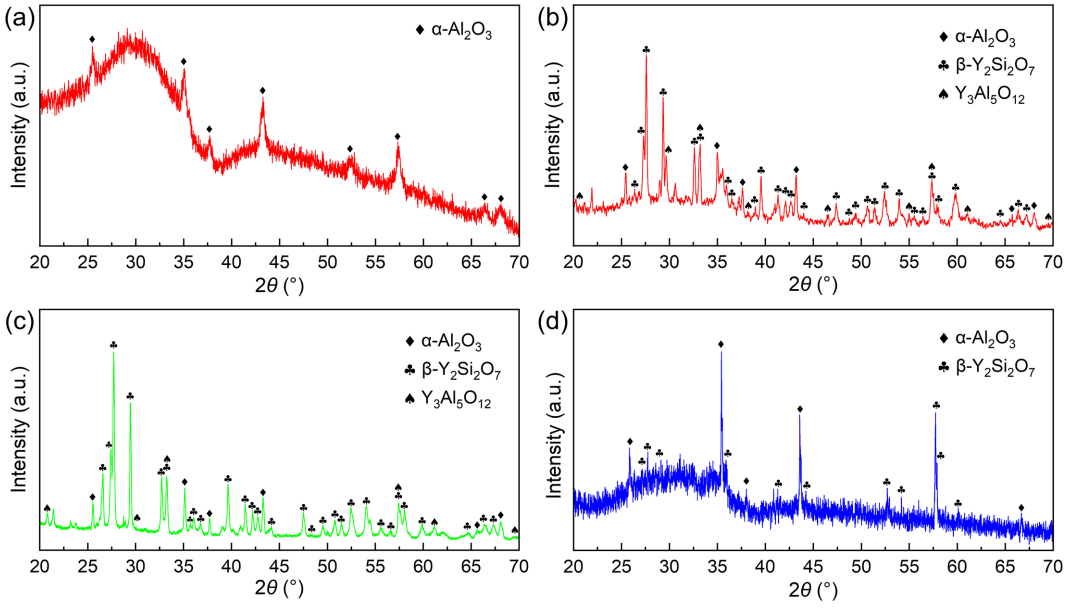

Fig. 4 XRD patterns of (a) as-received YAS glass and YAS glass fillers heat-treated under the same conditions as those used for joint fabrication at (b) J1400, (c) J1450, and (d) J1500.

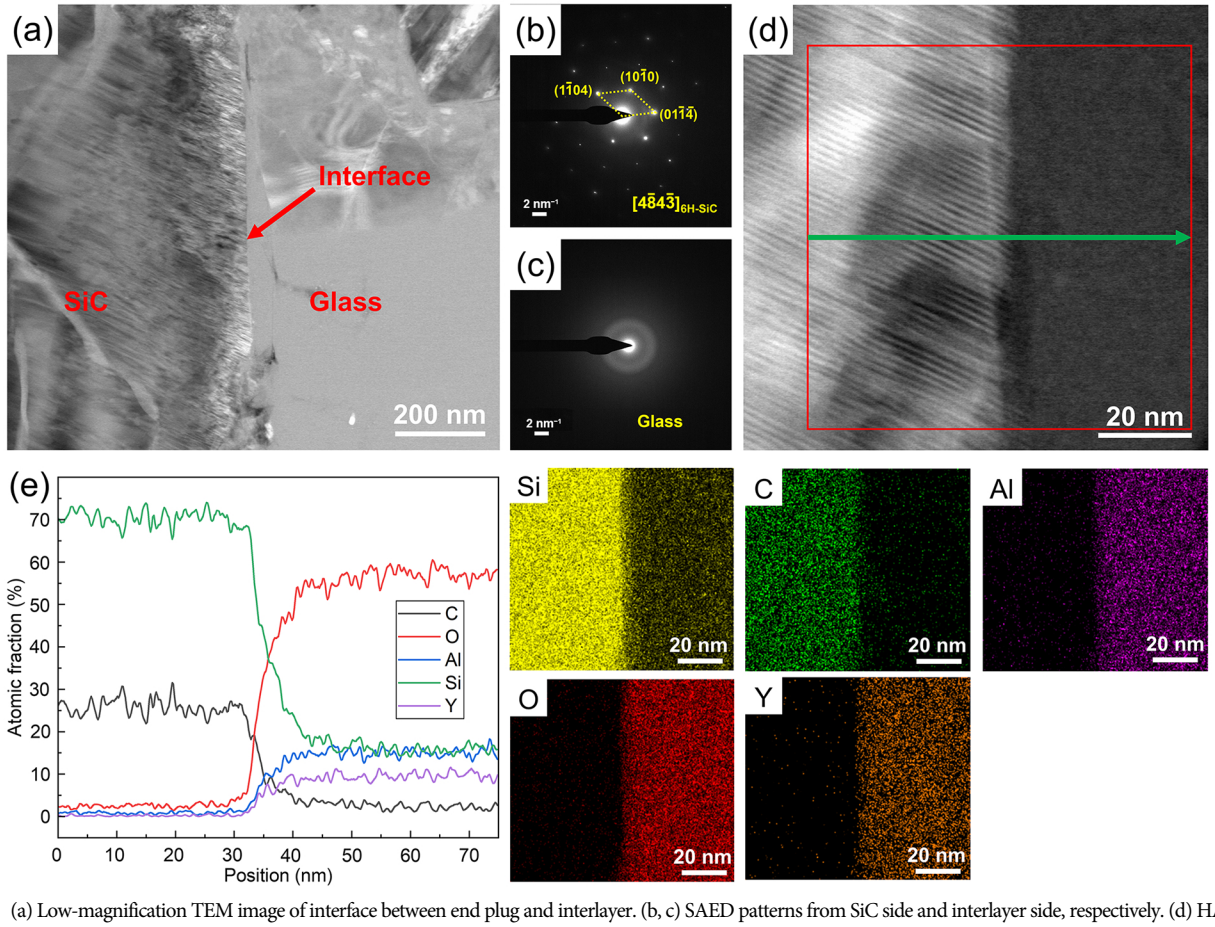

Fig. 5 (a) Low-magnification TEM image of interface between end plug and interlayer. (b, c) SAED patterns from SiC side and interlayer side, respectively. (d) HAADF image with corresponding EDS elemental maps. (e) EDS line profiles across interface along arrow in (d).

show crystalline SiC and an amorphous glass phase, respectively. Elemental mapping and line-scan analysis (Figs. 5(d) and 5(e)) indicate that Si and C are confined to the SiC side, while O, Al, and Y are enriched in the glass region. The compositional transition occurs over a narrow zone of approximately 5 nm, centered at approximately 33–38 nm in the line-scan profile, suggesting limited interdiffusion.

Figure 6 shows the microstructure of the interface between the interlayer and the cladding tube. The results reveal that the interlayer does not directly bond with the tube. Instead, a dark-colored interface phase is present, which forms indirect bonding between the interlayer and the SiC substrate. From the EDS elemental mapping in Fig. 6, it is evident that this interface phase does not show significant elemental signals from other elements but exhibits a strong carbon signal, indicating the presence of a carbon-rich phase. Further examination of the microstructure in Fig. 6 allows the identification of Regions A and B, where Region A represents the interface region between the interlayer and the carbon-rich phase, and Region B corresponds to the interface region between the carbon-rich phase and the SiC cladding tube. Figure 7(a) shows a low-magnification TEM image of region A, with the red arrow indicating the interface between the filler (on the left) and the carbon-rich phase (on the right). This interface is continuously bonded. Figure 7(b) displays the scanning transmission electron microscopy (STEM) images with corresponding SAED patterns of the interlayer, which reveal its amorphous nature. In contrast, Fig. 7(c) presents the STEM image of the carbon-rich phase, identified as PyC, which exhibits a disordered graphite-like structure. This is confirmed by the SAED pattern, which shows concentric diffraction rings with discernible brightness variations. Additionally, EDS elemental mapping of the interface region is shown in Fig. 7(d). The mapping results indicate that the elements Al, Y, and O are evenly distributed in the interlayer, while C is uniformly distributed on the PyC side. However, notable Si enrichment is observed at the interface, as indicated by the white arrows. This localized accumulation of Si

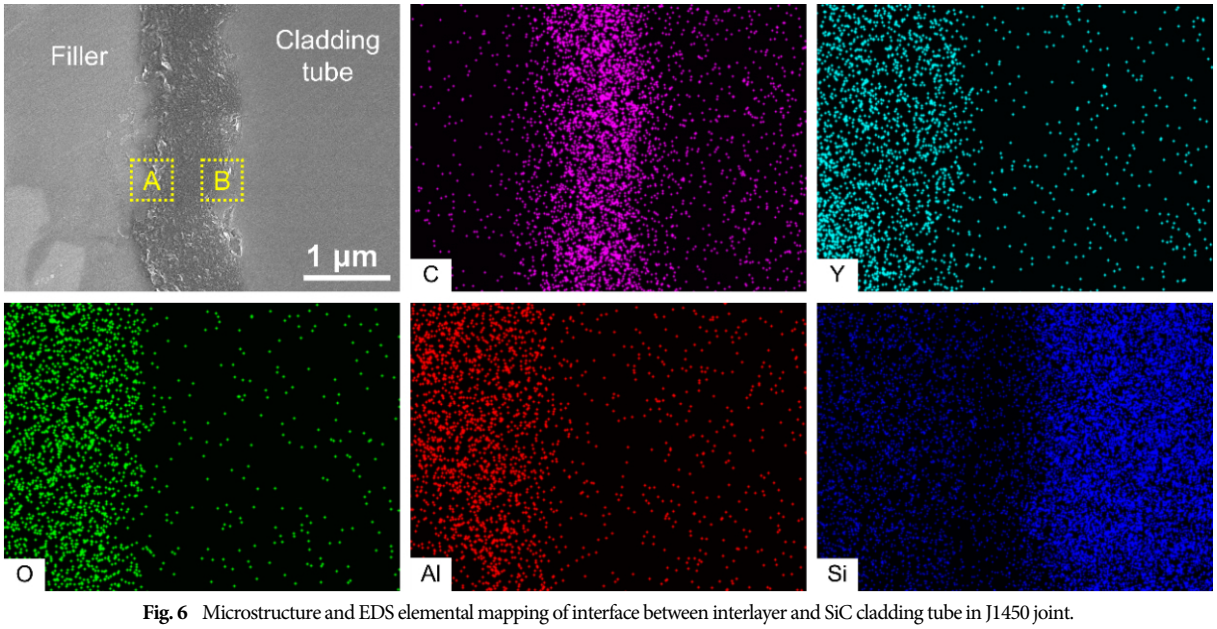

Fig. 6 Microstructure and EDS elemental mapping of interface between interlayer and SiC cladding tube in J1450 joint.

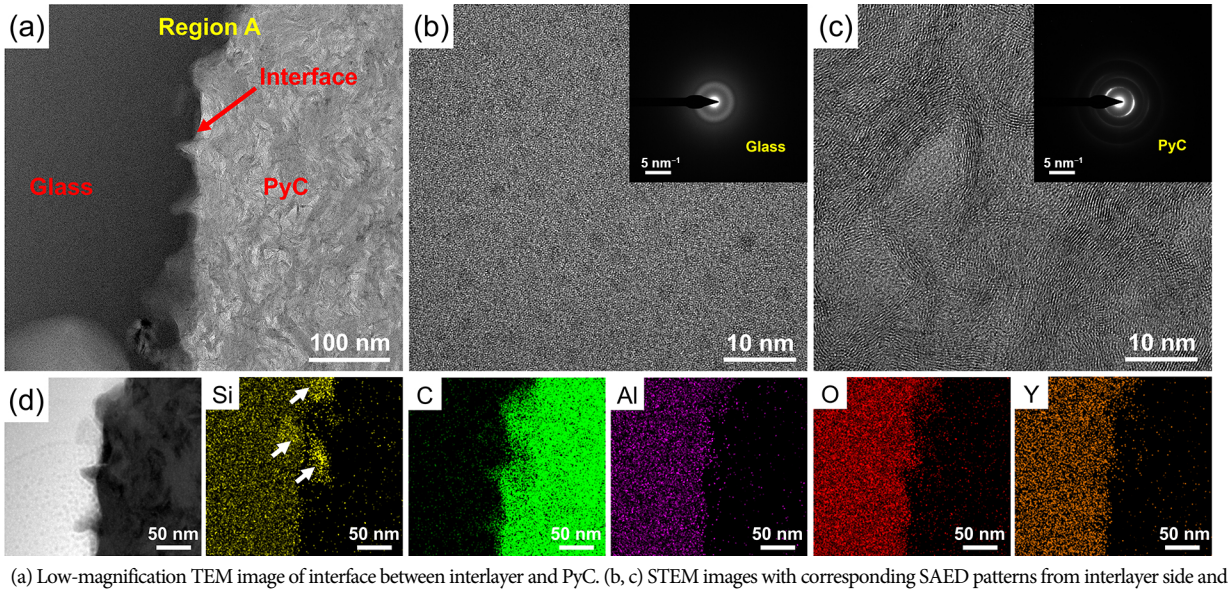

Fig. 7 (a) Low-magnification TEM image of interface between interlayer and PyC. (b, c) STEM images with corresponding SAED patterns from interlayer side and PyC side, respectively. (d) HAADF-STEM images with corresponding EDS elemental maps.

may be attributed to the diffusion of Si from the glass filler into the interface region during the high-temperature joining process. The lack of direct correlation between Si and O distribution suggests that Si accumulation is not primarily due to SiO_2 formation but rather to a diffusion or segregation process influenced by the joining conditions.

To investigate the origin of the PyC, we performed EDS point scanning and Raman analysis on the inner surface of the initial SiC cladding tube, as shown in Fig. 8. The inner surface of the cladding tube (Fig. 8(a)) exhibits convex granular features typical of the chemical vapor infiltration (CVI) process. EDS analysis at Spectrum 1 reveals 71.6 at% C and 28.4 at% Si, suggesting a carbon-rich surface layer attributed to residual PyC formed by transient gas-phase fluctuations during furnace cooling. The Raman spectrum (Fig. 8(b)) shows characteristic peaks at ~1342 cm^{-1} (D-band) and ~1574 cm^{-1} (G-band), further confirming the presence of PyC on the inner surface. These results demonstrate that the PyC phase observed at the interface between the SiC cladding tube and the filler originates from the residual PyC present on the inner surface of the initial SiC cladding tube.

Further TEM analysis of the interface between PyC and the SiC cladding tube was conducted (region B in Fig. 6), as shown in Fig. 9. Figure 9(a) displays a low-magnification TEM image, with the left side corresponding to PyC and the right side to SiC, where the interface exhibits good interfacial integrity. Figure 9(b) shows a STEM image with a corresponding SAED pattern from the SiC side, revealing the characteristic structure of 3C-SiC, which is as expected for this material. The elemental distribution was further investigated using EDS mapping, as shown in Fig. 9(c). The Si and C elements are evenly distributed on the SiC side, with minimal oxygen content. However, on the PyC side, a localized enrichment of Si and O is observed, as indicated by the white arrows, suggesting the possible formation of SiO_2-rich species. Notably, the interfacial region between PyC and SiC exhibits an enhanced oxygen signal, as highlighted by the blue arrows. This interfacial oxygen enrichment may originate from oxygen diffusion from the surrounding environment or the glass filler during the high-temperature joining process.

The nominal burst pressure of the J1400, J1450, and J1500 joints was evaluated by the EPPO test, and the results are

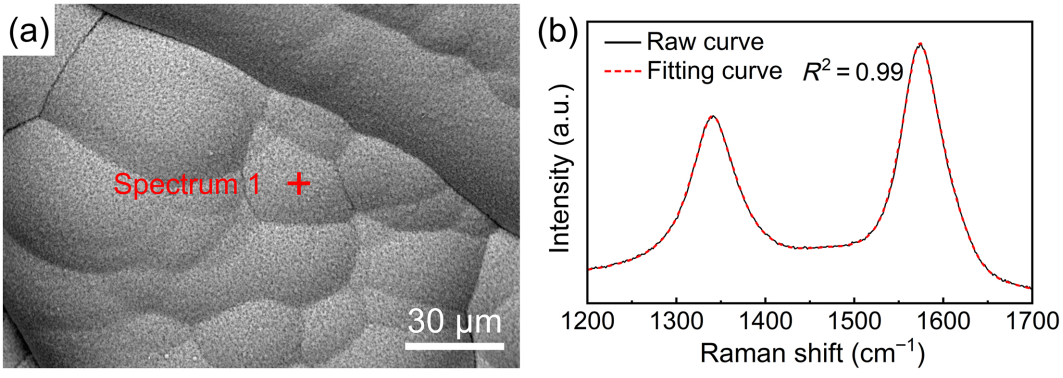

Fig. 8 (a) SEM image of inner surface of tube with EDS point analysis at Spectrum 1. (b) Raman spectrum of inner surface.

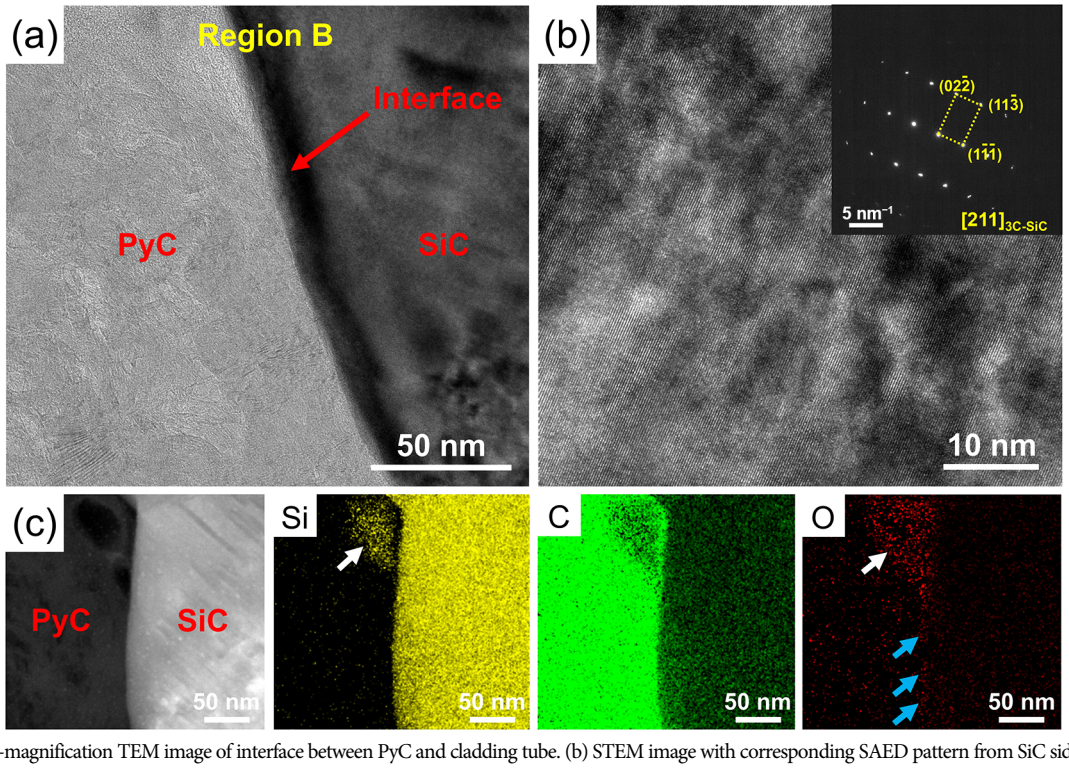

Fig. 9 (a) Low-magnification TEM image of interface between PyC and cladding tube. (b) STEM image with corresponding SAED pattern from SiC side. (c) HAADF-STEM images with corresponding EDS elemental maps.

summarized in Table 2. The J1400 joint exhibits the lowest nominal burst pressure of 41.9±8.6 MPa, with failure occurring mainly at the interface between the interlayer and the tube, as illustrated in Fig. 10(a). This behavior is consistent with the weak interfacial bonding and localized voids revealed in the microstructural observations, indicating that the interfacial bonding quality plays a dominant role in determining the mechanical performance of the joint. In contrast, the nominal burst pressure increased markedly to 70.3±10.0 MPa for J1450 and 68.9±10.5 MPa for J1500. At both 1450 and 1500 °C, joint failure is characterized by a mixed fracture mode involving the interface between the interlayer and the cladding tube itself (Fig. 10(b)), indicating that the interfacial bonding strength approaches the intrinsic strength of the cladding tube. These results indicate that increasing the joining temperature from 1400 to 1450–1500 °C effectively enhances joint strength by improving filler wetting and interfacial bonding. Herrmann *et al.* [29] previously joined SiC ceramic tubes using a laser-based localized rapid heating technique, obtaining nominal burst pressures in the range of 38.5–54.1 MPa. In this study, localized rapid induction heating was employed to join SiC_f/SiC cladding tubes, resulting in joints with an even higher nominal burst pressure (70.3±10.0 MPa). The results considerably exceed the maximum nominal internal pressure (15.5 MPa) expected at the end of life for PWR fuel rods [19], highlighting the promising potential of the present localized induction joining technique for nuclear-grade sealing applications. It should be noted that most previous studies focused on joining SiC_f/SiC blocks or tubular specimens evaluated using different mechanical testing methods, whereas systematic end-plug push-out testing data for SiC_f/SiC cladding tube joints are still scarce. As a result, direct quantitative comparison of joint strength among different studies is challenging due to differences in specimen geometry, testing standards, and strength calculation models.

3.2 Interfacial hydrothermal corrosion behavior of the J1450 joint

Among all joints, J1450 exhibited the most compact interface and uniform phase distribution, together with the highest nominal burst pressure. Therefore, it was selected for hydrothermal corrosion evaluation. Figures 11(a) and 11(b) show the interfacial microstructures between the end plug (left) and the interlayer (right) before and after hydrothermal corrosion for 9 days, respectively. Before corrosion, the interface was well bonded, showing no discernible pores or signs of delamination (blue arrow in Fig. 11(a)). After 9 d of exposure, however, clear evidence of interfacial degradation appeared (Fig. 11(b)). The enlarged view of the yellow-dashed box region, presented in Fig. 11(c), reveals newly formed interfacial pores (red arrows), indicating localized corrosion-induced damage along the interface. A comparison between Figs. 11(a) and 11(b) further indicates that corrosion mainly occurred on the interlayer side of the interface, where the filler was preferentially degraded.

To further characterize the surface topography at the interface between the SiC end plug and the interlayer, AFM was performed before and after hydrothermal corrosion. Figures 12(a) and 12(b) present the AFM images of the end plug and the adjacent interlayer prior to corrosion. Both surfaces are relatively flat and continuous, showing only nanoscale roughness. The surface of the interlayer lies approximately 50 nm below that of the SiC end plug. This small step difference results from the lower hardness of the glass–ceramic interlayer compared with SiC, leading to slightly greater material removal during polishing [30]. After hydrothermal corrosion, the surface morphology of the interlayer changes markedly (Figs. 12(c) and 12(d)). The roughness increases significantly, especially near the interface. The results show that the interlayer surface, originally ~50 nm lower than the SiC end plug surface, becomes recessed by an additional ~300 nm

Table 2 Nominal burst pressure and failure modes of the joints

Joint	Nominal burst pressure (MPa)	Failure mode
J1400	41.9±8.6	Interface between interlayer and cladding tube
J1450	70.3±10.0	Interlayer + SiC_f/SiC
J1500	68.9±10.5	Interlayer + SiC_f/SiC
J1450 (after corrosion)	62.4±7.6	Interlayer + SiC_f/SiC

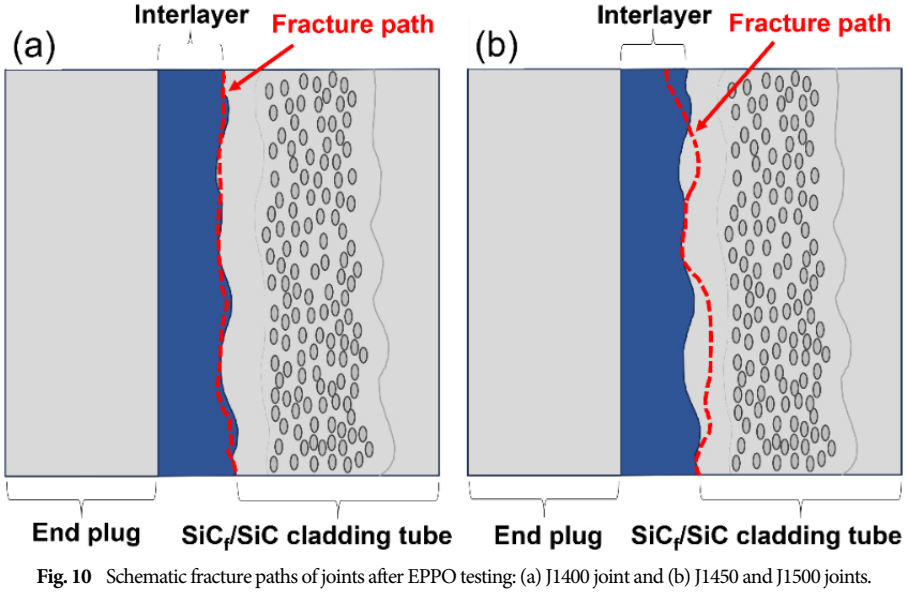

Fig. 10 Schematic fracture paths of joints after EPPO testing: (a) J1400 joint and (b) J1450 and J1500 joints.

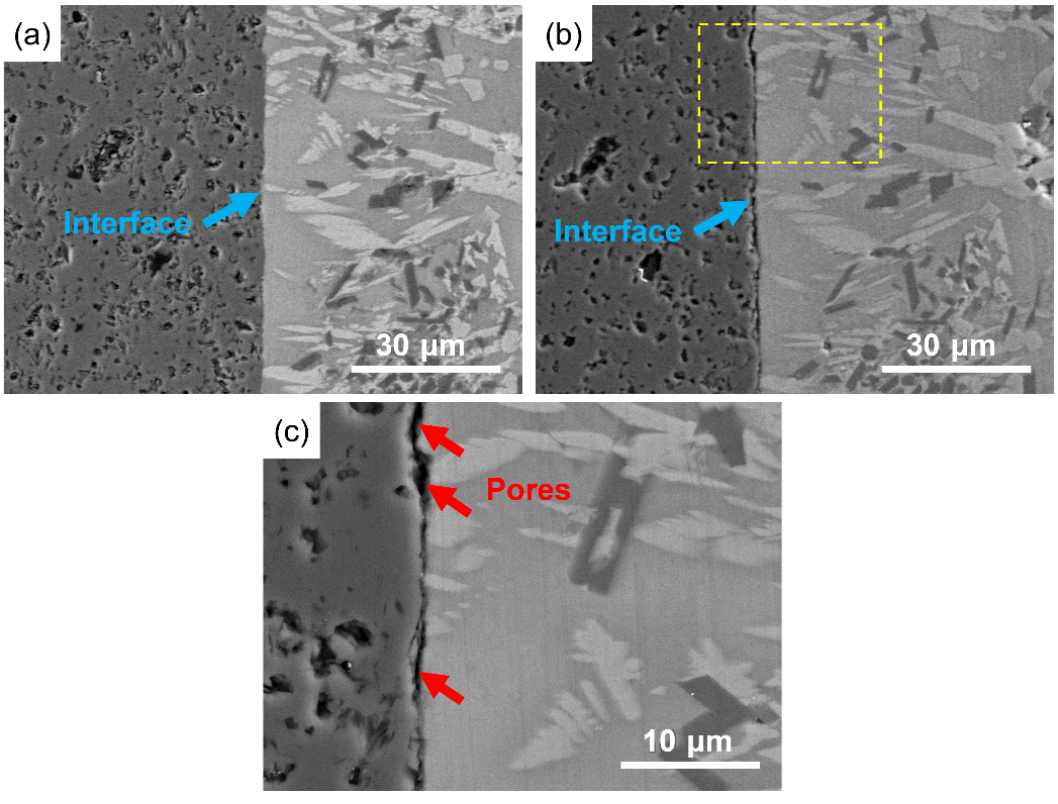

Fig. 11 SEM images of interface between end plug and interlayer: (a) before corrosion, (b) after 9 d of hydrothermal corrosion, and (c) enlarged view of yellow dashed region in (b).

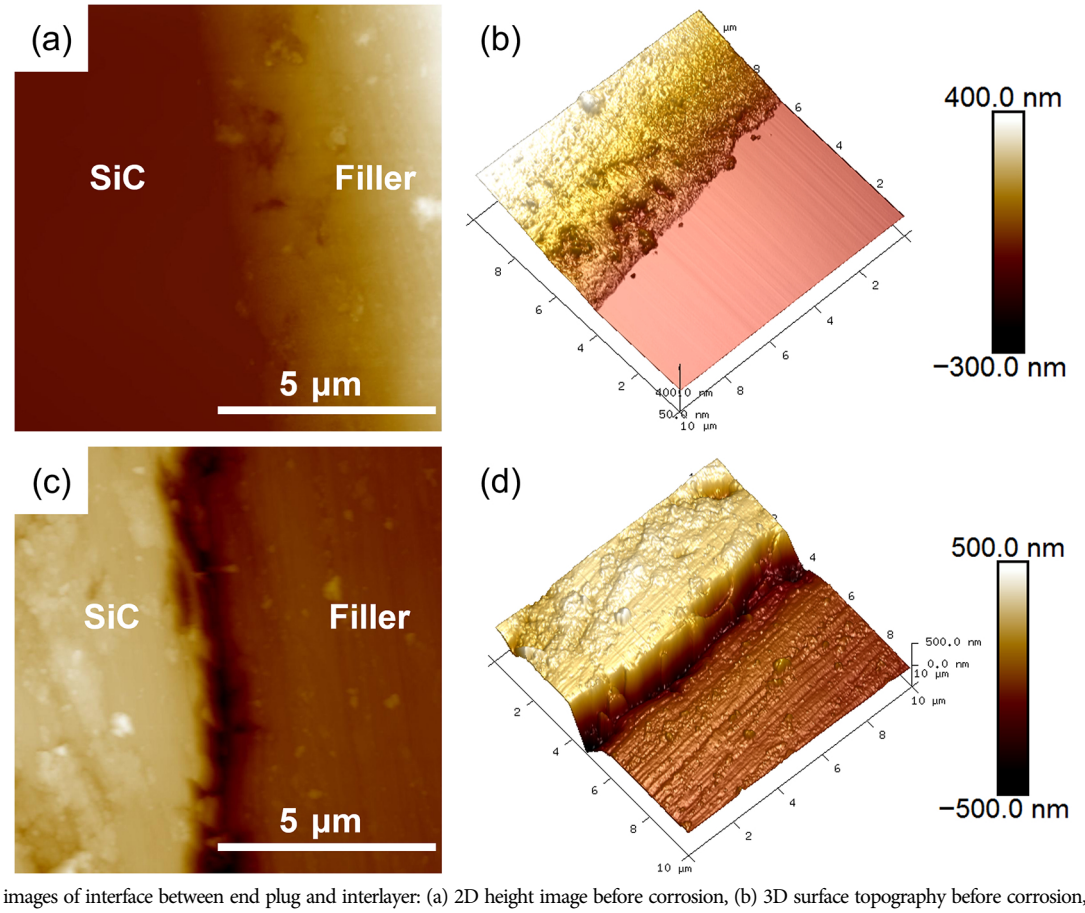

Fig. 12 AFM images of interface between end plug and interlayer: (a) 2D height image before corrosion, (b) 3D surface topography before corrosion, (c) 2D height image after corrosion, and (d) 3D surface topography after corrosion.

after corrosion, indicating dissolution of the glassy matrix. To further elucidate the dominant factors governing the corrosion degradation of the interlayer, a bulk YAS glass specimen prepared at 1450 °C was subjected to hydrothermal corrosion, and the aqueous solution was subsequently collected for elemental concentration analysis. The results are summarized in Table 3. The concentration of Y in the solution is the lowest, at 38.5 ppb, while the Al concentration is higher by approximately one order of magnitude, reaching 200 ppb. In contrast, Si exhibits the highest concentration, reaching 491 ppb. These results indicate that Si is preferentially dissolved in the present glass–ceramic system, suggesting that Si-containing structural units represent the weakest link with respect to hydrothermal corrosion. The interfacial region is further depressed by approximately 600 nm relative to the end plug surface, reflecting locally accelerated degradation at the interface.

The degradation feature on the end plug side of the joint is schematically illustrated in Figs. 13(a) and 13(b), showing that while the interlayer undergoes overall recession due to corrosion, the interfacial zone suffers more severe localized attack, resulting in a deeper depression at the interface. Depth-profile analysis confirms that corrosion penetrates several hundred nanometers into the interlayer, whereas the end plug remains smooth and intact, underscoring its superior resistance to hydrothermal corrosion. In addition to the inherent material mismatch, the localized rapid induction heating process, with its accelerated heating and cooling rates, may induce complex residual stress states at the interface and further exacerbate interfacial corrosion. A quantitative assessment of the residual stress level and its detailed correlation with localized induction heating parameters requires dedicated experimental and modeling investigations.

Figures 14(a) and 14(b) show the interfacial microstructures between the interlayer (left) and the cladding tube (right) before and after hydrothermal corrosion, respectively. Before corrosion, a thin dark interfacial layer can be clearly observed between the filler and the tube (the yellow arrow in Fig. 14(a)), the nature of which will be discussed later. After 9 d of exposure, partial depletion or detachment of the dark layer occurs at the interface, leading to localized debonding (the yellow arrow in Fig. 14(b)). The enlarged view of the yellow dashed region in Fig. 14(b), shown in Fig. 14(c), further reveals newly formed interfacial pores (the red arrows), indicating that corrosion-induced degradation is concentrated at the interface.

Table 3 Elemental concentrations in solution after corrosion of filler prepared at 1450 °C

Element	Concentration (ppb)
Y	38.5
Al	200
Si	491

Figures 15(a) and 15(b) show AFM images of the interface between the SiC_f/SiC cladding tube and the interlayer prior to corrosion. The glass filler and the cladding tube are bonded through a PyC interfacial layer, which is clearly visible. The surface of the interlayer lies approximately 20 nm below the adjacent cladding tube surface, consistent with the lower hardness and polishing resistance of the glass–ceramic interlayer. After 9 d of hydrothermal corrosion (Figs. 15(c) and 15(d)), the surface morphology changed markedly. The surface of the interlayer becomes considerably rougher, and corrosion pits appear preferentially at the interface. The interlayer surface lies ~400 nm below the adjacent cladding tube surface, reflecting significant overall recession of the interlayer. Depth profile analysis revealed that these interfacial cavities extend to depths of up to ~5 μm, confirming severe localized penetration along the interface.

Previous studies reported that the hydrothermal stability of PyC remains a critical concern in SiC_f/SiC composites [31,32]. Under hydrothermal conditions, PyC undergoes oxidation–reduction reactions (Eq. (3)) [33]. Moreover, residual stresses at the joint interface may also contribute to PyC degradation and interfacial debonding. Although these stresses were not quantitatively evaluated in the present work, their characterization is an important objective of our future studies. This degradation scenario is schematically illustrated in Figs. 16(a) and 16(b), showing that while the glass–ceramic interlayer undergoes pronounced surface recession, the PyC interface experiences much deeper localized degradation, resulting in extensive interfacial penetration under hydrothermal attack. In addition, Si enrichment is observed at the filler/PyC interface, while SiO_2 is present at the PyC/SiC interface. Such interfacial chemical heterogeneity may be detrimental to the maintenance of the hydrothermal corrosion resistance of the joints.

$$C + H_2O \rightarrow CO + H_2 \quad (3)$$

Compared with the interface between the end plug and the interlayer, the interface between the cladding tube and the interlayer exhibited more severe degradation. This difference may be primarily due to the PyC on the inner surface of the cladding tube, which is more vulnerable to hydrothermal attack. PyC may undergo oxidation–reduction reactions with water, leading to its

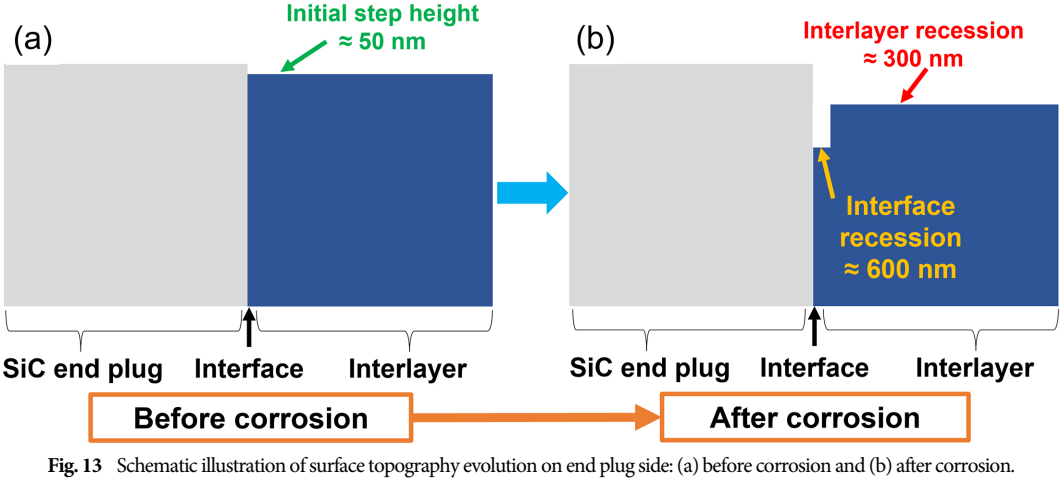

Fig. 13 Schematic illustration of surface topography evolution on end plug side: (a) before corrosion and (b) after corrosion.

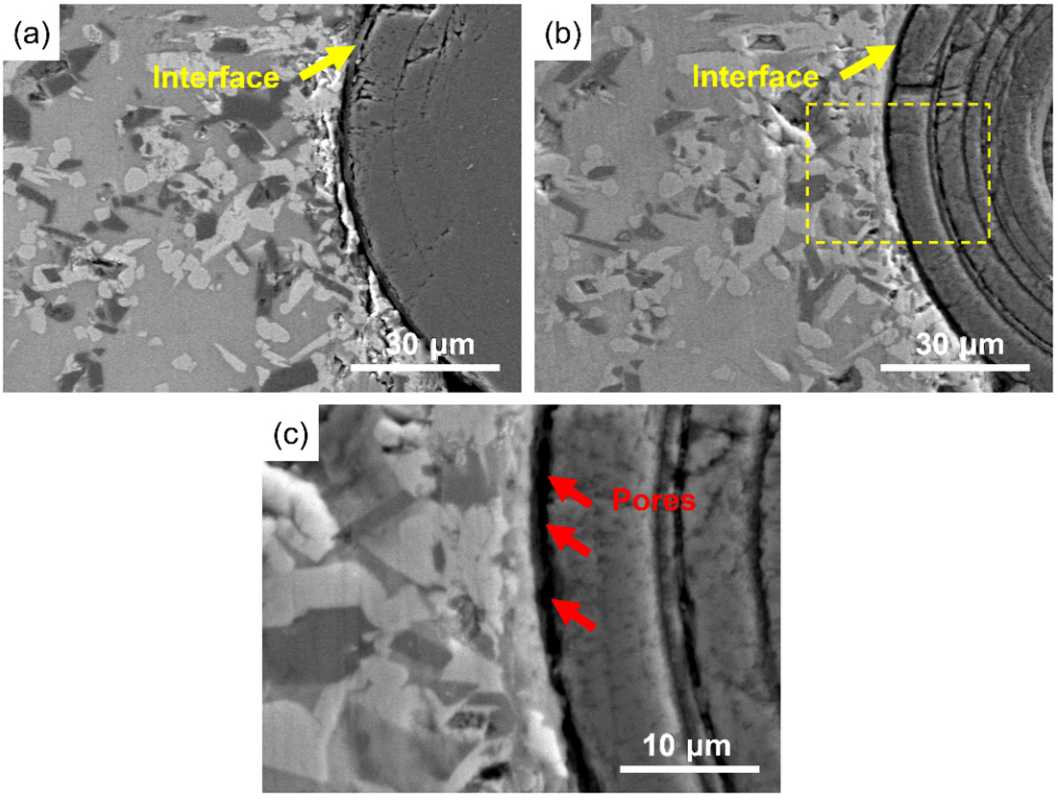

Fig. 14 SEM images of interface between interlayer and cladding tube in J1450 joint: (a) before corrosion; (b) after 9 d of hydrothermal corrosion; and (c) enlarged view of yellow dashed region in (b).

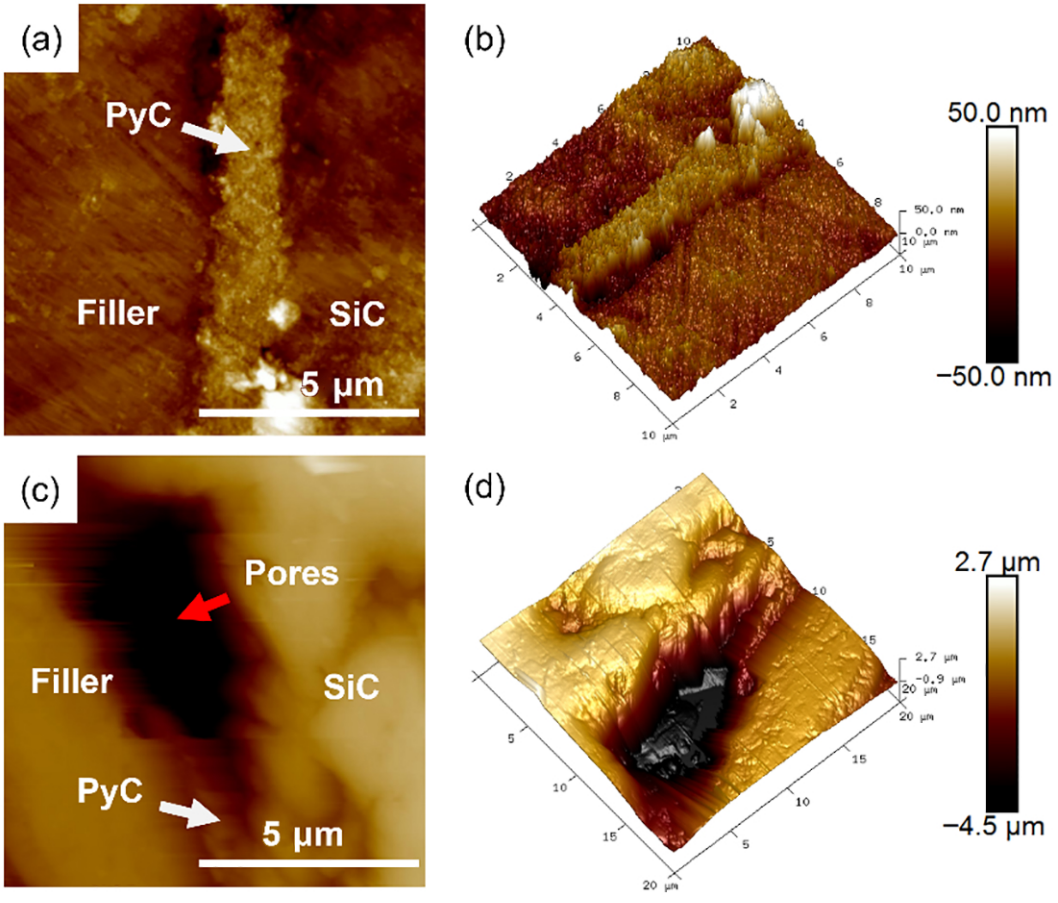

Fig. 15 AFM images of interface between tube and interlayer: (a) 2D height image before corrosion, (b) 3D surface topography before corrosion, (c) 2D height image after corrosion, and (d) 3D surface topography after corrosion.

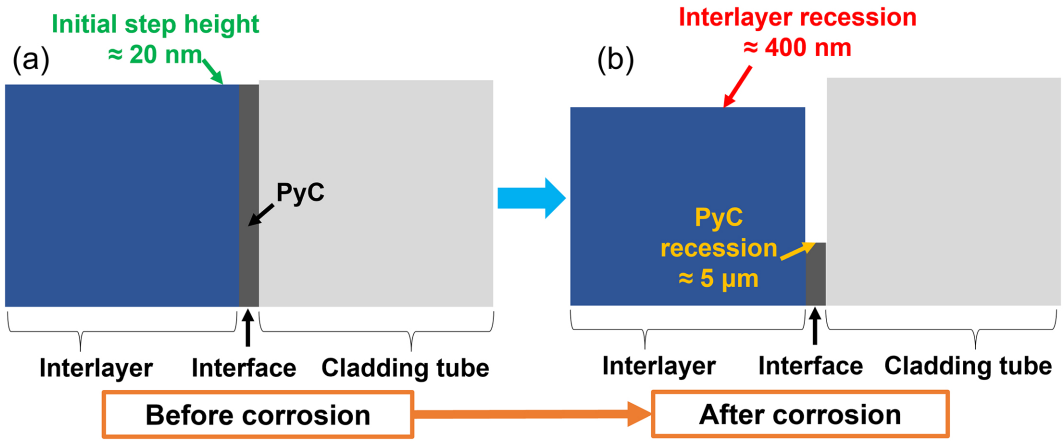

Fig. 16 Schematic illustration of surface topography evolution on tube side: (a) before corrosion and (b) after corrosion.

degradation. Breakdown of the PyC interphase results in interfacial voids that facilitate fluid ingress and accelerate dissolution of the adjacent filler, thereby compromising overall interfacial integrity. Consequently, after 9 d of hydrothermal corrosion, the nominal burst pressure of the J1450 joint decreased slightly to 62.4±7.6 MPa (Table 2), corresponding to a modest reduction of ~11% relative to the uncorroded joint.

4 Conclusions

SiC_f/SiC cladding tubes were successfully joined to SiC end plugs using a YAS glass filler through localized rapid heating. Among the investigated joining temperatures (1400–1500 °C), the joint fabricated at 1450 °C demonstrated the most favorable interfacial bonding and a uniformly distributed crystalline microstructure, primarily composed of $Y_2Si_2O_7$, $Y_3Al_5O_{12}$, and Al_2O_3, and achieved the highest nominal burst pressure of 70.3±10.0 MPa. At 1500 °C, crystallization of the YAS filler was suppressed, resulting in a glassy and heterogeneous interlayer. Hydrothermal corrosion of the J1450 joint revealed that the interfaces degrade more rapidly than the interlayer. On the cladding tube side, the interlayer forms an indirect bond with the tube, mediated by a PyC layer on the inner surface. This PyC-mediated interface is vulnerable under hydrothermal conditions, leading to accelerated corrosion. These results demonstrate that localized rapid joining is a viable strategy for sealing SiC_f/SiC cladding tubes, while the hydrothermal durability of the joint is governed primarily by the interfacial structure on the cladding tube side. Effective control of interfacial chemistry, particularly minimizing PyC and related interfacial heterogeneities, is therefore essential for improving the hydrothermal corrosion resistance and long-term reliability of SiC_f/SiC cladding tube joints.

Acknowledgements

This work was financially supported by the National Natural Science Foundation of China (Grant No. 52572069 and U24B2028), the Natural Science Foundation of Guangdong Province (No. 2024A1515011128), and the Science and Technology Innovation Program of Hunan Province (No. 2025RC4025). The authors would like to thank the Instrumental Analysis Center of Guangdong University of Technology for its support.

Availability of data and materials

The data that support the findings of this study are available from the corresponding author upon reasonable request.

Competing interests

The authors have no competing interests to declare that are relevant to the content of this article. The author Hua-Tay Lin is the Editor-in-Chief of this journal.

References

[1] Yang JS, Ye F, Cheng LF, *et al.* Preparation and properties of Ti_3SiC_2-based corrosion mitigation coatings for SiC_f/SiC PWR accident tolerant fuel cladding. *J Adv Ceram* 2024, **13**: 73–85.
[2] Zhan L, Bo Y, Lin T, *et al.* Development and outlook of advanced nuclear energy technology. *Energy Strateg Rev* 2021, **34**: 100630.
[3] Liu SJ, Qiu HP, Xu P, *et al.* Effect of different sewing density on mechanical properties of 2D SiC/SiC composites. *Adv Ceram* 2025, **46**: 52–62. (in Chinese)
[4] Zhang JF, Zhao L, Yang JL, *et al.* Synergistic damage behavior of He ion irradiation and molten salt corrosion in SiC at 750 °C. *J Adv Ceram* 2024, **13**: 1786–1794.
[5] Ferraris M, Salvo M, Casalegno V, *et al.* Joining of SiC-based materials for nuclear energy applications. *J Nucl Mater* 2011, **417**: 379–382.
[6] Henager CH, Shin Y, Blum Y, *et al.* Coatings and joining for SiC and SiC-composites for nuclear energy systems. *J Nucl Mater* 2007, **367**: 1139–1143.
[7] Zhao CC, Lin RL, Dai MM, *et al.* Facile joining of SiC ceramics with screen-printed polycarbosilane without pressure. *J Eur Ceram Soc* 2021, **41**: 2157–2161.
[8] Fang J, Sun LB, Guo SS, *et al.* Study of Li_2O addition on crystallization behavior and thermal expansion properties of $CaO–Al_2O_3–SiO_2$ (CAS) glass–ceramic and its application for joining SiC ceramic. *J Eur Ceram Soc* 2021, **41**: 1817–1827.
[9] Fitriani P, Kwon H, Zhou XB, *et al.* Joining of SiC_f/SiC using a layered $Ti_3SiC_2–SiC_w$ and TiC gradient filler. *J Eur Ceram Soc* 2020, **40**: 1043–1051.
[10] Zhan CT, He SJ, Guo WM, *et al.* Joining of SiC ceramics by combining NITE–SiC interlayer and its thickness control. *J Eur Ceram Soc* 2023, **43**: 3070–3076.
[11] Singh M. Microstructure and mechanical properties of reaction-formed joints in reaction-bonded silicon carbide ceramics. *J Mater Sci* 1998, **33**: 5781–5787.
[12] Fitriani P, Iskandar F, Colkesen P, *et al.* Pressureless joining of SiC by molten Si infiltration to the SiC/C filler tape and residual stress analysis. *J Eur Ceram Soc* 2024, **44**: 5370–5379.
[13] Golosov MA, Utkin AV, Lozanov VV, *et al.* Joining of SiC ceramics by iridium: The interfacial phenomena and joint strength. *Ceram Int* 2024, **50**: 51447–51455.
[14] Sun LB, Hou CM, Yang HT, *et al.* Reaction behavior and mechanical performance of SiC_f/SiC brazed joint using Si–Y eutectic alloy. *J Eur Ceram Soc* 2025, **45**: 117697.

[15] Fang J, Zhang J, Liu CF, *et al.* A novel glass–ceramic with high crystallinity for joining of SiC ceramic. *Mater Lett* 2020, **277**: 128318.
[16] Katoh Y, Snead LL, Cheng T, *et al.* Radiation-tolerant joining technologies for silicon carbide ceramics and composites. *J Nucl Mater* 2014, **448**: 497–511.
[17] Sun LB, Wang SH, Hou CM, *et al.* Microstructure, mechanical property and bonding mechanism of SiC ceramic joint using a novel $Y_2Si_2O_7$/mullite glass–ceramic interlayer. *Ceram Int* 2023, **49**: 17885–17893.
[18] Malinverni C, Salvo M, Ziętara M, *et al.* A yttrium aluminosilicate glass–ceramic to join SiC/SiC composites. *J Eur Ceram Soc* 2024, **44**: 3579–3587.
[19] Wang L, Fan SW, Sun HD, *et al.* Pressure-less joining of SiC_f/SiC composites by Y_2O_3–Al_2O_3–SiO_2 glass: Microstructure and properties. *Ceram Int* 2020, **46**: 27046–27056.
[20] Yang SB, Meng XY, Chen B, *et al.* Encapsulation of SiC/SiC cladding tubes with excellent mechanical performance and air tightness using a CaO-modified Y_2O_3–Al_2O_3–SiO_2 glass. *Ceram Int* 2024, **50**: 29850–29858.
[21] Wu LX, Xue JX, Liao YH, *et al.* Connection method for silicon carbide cladding for nuclear application, and silicon carbide cladding and application thereof. WO patent WO 2022205782A1, Oct. 2022.
[22] Ma YJ, Yang SB, Meng XY, *et al.* Corrosion behavior and mechanism of the Y_2O_3–Al_2O_3–SiO_2 system during long-term corrosion in water-oxygen environment at 1350 °C. *Ceram Int* 2023, **49**: 28344–28353.
[23] Ma YJ, Guo C, Meng XY, *et al.* Enhanced thermal shock resistance of SiC_f/SiC composites with Y–Al–Si–O glass ceramic environmental barrier coatings in water-oxygen conditions at 1350 °C. *J Eur Ceram Soc* 2025, **45**: 116956.
[24] Otero N. Laser surface modification to enhance brazing joints. *J Laser Micro Nanoen* 2013, **8**: 137–143.
[25] Ma CH, Bai SX, Peng XD, *et al.* Improving hydrophobicity of laser textured SiC surface with micro-square convexes. *Appl Surf Sci* 2013, **266**: 51–56.
[26] Sun Z, Chen X, Mao Y, *et al.* Joining of SiC ceramics using CaO–Al_2O_3–SiO_2 (CAS) glass ceramics. *J Eur Ceram Soc* 2020, **40**: 267–275.
[27] Fu W, Xue YD, Song XG, *et al.* Microstructural evolution and mechanical properties of Al_2O_3/Al joint bonded by Bi_2O_3–B_2O_3–SiO_2–ZnO–Al_2O_3 glass. *Ceram Int* 2025, **51**: 612–622.
[28] Dehm G, Inkson BJ, Wagner T. Growth and microstructural stability of epitaxial Al films on (0001) α-Al_2O_3 substrates. *Acta Mater* 2002, **50**: 5021–5032.
[29] Herrmann M, Lippmann W, Hurtado A. High-temperature stability of laser-joined silicon carbide components. *J Nucl Mater* 2013, **443**: 458–466.
[30] Sun LB, Liu CF, Fang J, *et al.* Multiscale characterization of damage behavior of glass–ceramic bonded SiC joint under He ion irradiation. *J Eur Ceram Soc* 2024, **44**: 1946–1958.
[31] Koyanagi T, Katoh Y, Nozawa T. Design and strategy for next-generation silicon carbide composites for nuclear energy. *J Nucl Mater* 2020, **540**: 152375.
[32] Seshadri A, Phillips B, Shirvan K. Impact of nuclear environment on hydrothermal corrosion and silica transport for CVD SiC in light water reactors. *J Nucl Mater* 2021, **556**: 153155.
[33] Biscay N, Henry L, Adschiri T, *et al.* Behavior of silicon carbide materials under dry to hydrothermal conditions. *Nanomaterials* 2021, **11**: 1351.